

# Temporal solitons in optical microresonators

T. Herr<sup>1</sup>, V. Brasch<sup>1</sup>, J. D. Jost<sup>1</sup>, C. Y. Wang<sup>1</sup>, N. M. Kondratiev<sup>2</sup>, M. L. Gorodetsky<sup>2,3\*</sup>  
and T. J. Kippenberg<sup>1\*</sup>

**Temporal dissipative solitons in a continuous-wave laser-driven nonlinear optical microresonator were observed. The solitons were generated spontaneously when the laser frequency was tuned through the effective zero detuning point of a high-Q resonance, which led to an effective red-detuned pumping. Transition to soliton states were characterized by discontinuous steps in the resonator transmission. The solitons were stable in the long term and their number could be controlled via pump-laser detuning. These observations are in agreement with numerical simulations and soliton theory. Operating in the single-soliton regime allows the continuous output coupling of a femtosecond pulse train directly from the microresonator. This approach enables ultrashort pulse syntheses in spectral regimes in which broadband laser-gain media and saturable absorbers are not available. In the frequency domain the single-soliton states correspond to low-noise optical frequency combs with smooth spectral envelopes, critical to applications in broadband spectroscopy, telecommunications, astronomy and low noise microwave generation.**

Temporal dissipative solitons<sup>1,2</sup> can exist stably in a nonlinear cavity for an infinite amount of time when a continuous-wave (c.w.) pump laser is coupled to the cavity. Essentially, these solitons rely on the double balance between anomalous cavity dispersion and Kerr nonlinearity on the one hand, and cavity loss and parametric frequency conversion of the pump light on the other<sup>3,4</sup>. Mathematically, the system is described by the Lugiato–Lefever equation<sup>5</sup> (damped, driven nonlinear Schrödinger equation), to which temporal dissipative cavity solitons on top of a weak c.w. field at the pump frequency are stable solutions<sup>3,6</sup>. It is worthwhile emphasizing that dissipative cavity solitons are different from dissipative solitons in lasers, which already find widespread use<sup>2</sup>. Although the spatial analogue<sup>7–9</sup> of temporal dissipative cavity solitons has been observed frequently in experiments, only recently have temporal dissipative cavity solitons been observed experimentally in fibre cavities<sup>4</sup>. Here, the solitons were induced by external writing pulses coupled to the cavity. It has been suggested that these temporal dissipative solitons may also be supported by high-quality factor (Q) nonlinear optical microresonators<sup>4,10</sup>. Recently, these microresonators<sup>11,12</sup> have been attracting growing attention in the scientific community and, in particular, microresonator-based frequency-comb generation has, within a few years, evolved into a research field of its own<sup>13–19</sup>. For frequency comb generation, a c.w. pump laser is coupled to the microresonator where cascaded four-wave mixing (FWM) can give rise to equidistant and coherent optical lines with a spacing that corresponds to the free spectral range (FSR, typically several gigahertz up to terahertz) of the microresonator (Fig. 1c, inset). Although it has been shown that these FWM-based microresonator combs can perform on a level required for optical-frequency metrology applications<sup>18,20,21</sup>, these systems often suffer from significant frequency and amplitude noise<sup>22–25</sup> and, unlike conventional mode-locked laser-based frequency combs, do not correspond to ultrashort pulses in the time domain. The latter can be understood by the constant but arbitrary phase relations between the comb lines, which result from the formation process (Fig. 1c)<sup>22</sup>. External line-by-line phase and amplitude adjustment may be used after comb generation for pulse shaping<sup>23,24</sup>, but this is restricted to only a small number of comb

modes. Very recently, direct ultrashort pulse generation in a Si<sub>3</sub>N<sub>4</sub> microresonator was observed but is to date unexplained<sup>26</sup>. In a different, but related, system that comprises a fibre cavity with laser gain and a nonlinear high-index silica microresonator in filter configuration, the generation of picosecond pulses with a high repetition rate was observed<sup>27</sup>.

In a strongly driven nonlinear microresonator, the resonance frequency is shifted towards lower frequencies by the Kerr nonlinearity when the intracavity power increases (Fig. 1c). An additional resonance shift results from thermal expansion and thermal refractive-index change (induced by absorptive heating). The thermal resonance shift occurs on a much slower timescale (thermal relaxation time) compared to the quasi-instantaneous Kerr shift. The combined Kerr-nonlinear and thermal resonance shifts manifest themselves in a non-Lorentzian, triangular resonance shape when the pump laser is scanned with decreasing optical frequency over the resonance (Fig. 2a, inset)<sup>12,28,29</sup>. These resonance shifts also result in a bistable behaviour, that is, two possible stable solutions for the intracavity power can exist for a particular pump laser detuning (see Fig. 1c). The solution with higher intracavity power is realized when the cavity is effectively blue detuned (pump frequency higher than the shifted resonance frequency). This detuning regime is self-stable as a result of a negative feedback between fluctuations in the effective detuning and resulting resonance shift<sup>29</sup>. The self-stability is exploited in microresonator-based frequency-comb generation in which, effectively, the pump laser is operated blue detuned. A stable effectively red-detuned operation is only possible for a large detuning, but usually is not considered because of the low intracavity power levels<sup>29</sup>.

## Results

In this work, we show that tuning the pump laser from the effectively blue-detuned regime through the effective zero detuning frequency into the effectively red-detuned regime can lead to the formation of temporal dissipative cavity solitons in a microresonator. The soliton regime is qualitatively different from the blue-detuned operating regime used so far in microresonator-based frequency combs. In contrast to fibre-cavity experiments<sup>4</sup>, the soliton

<sup>1</sup>École Polytechnique Fédérale de Lausanne, 1015 Lausanne, Switzerland, <sup>2</sup>Faculty of Physics, M. V. Lomonosov Moscow State University, Moscow 119991, Russia, <sup>3</sup>Russian Quantum Center, Skolkovo 143025, Russia. \*e-mail: michael.gorodetsky@gmail.com; tobias.kippenberg@pfl.ch

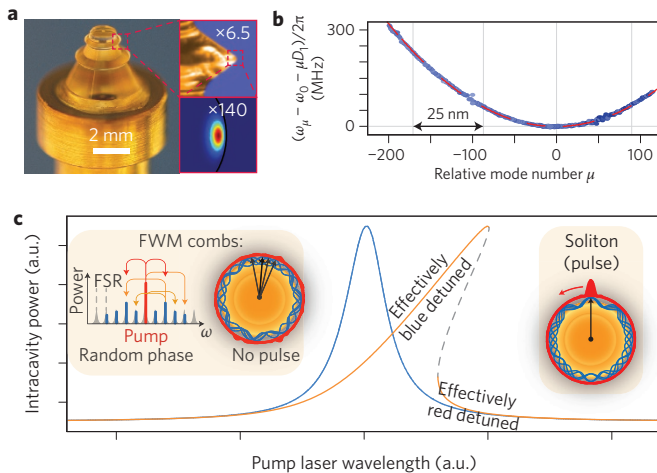


**Figure 1 |  $\text{MgF}_2$  microresonator, dispersion and bistability.** **a**,  $\text{MgF}_2$  crystal carrying two whispering-gallery-mode microresonators of different size (the smaller one with an FSR of 35.2 GHz was used). An optical whispering-gallery-mode propagates along the circumference of the resonator. The smaller panels show a magnified view of the resonator and the simulated optical mode profile. **b**, Anomalous dispersion (FSR increases with mode number) of the microresonator with 35.2 GHz FSR shown as the deviation of the measured resonance frequencies (blue dots),  $\omega_\mu = \omega_0 + D_1\mu + \frac{1}{2}D_2\mu^2 + \dots$ , from an equidistant frequency grid  $\omega_0 + \mu D_1$  (horizontal grey line), where  $\mu$  denotes the relative mode number and  $D_1$  corresponds to the FSR at the frequency  $\omega_0$ . The resonator's anomalous dispersion is described accurately by  $D_2/2\pi \approx 16$  kHz (red dashed line) while higher order terms are negligible. The grey vertical lines mark spectral intervals of width 25 nm ( $\mu = 0$  corresponds to 1,553 nm). **c**, Bistable intracavity power as a function of laser detuning for a linear (blue) and a nonlinear resonator (orange). The dashed line marks an unstable regime. The effectively blue-detuned and the effectively red-detuned regimes are indicated. In FWM combs the phases of the comb lines are constant but random, which leads to a periodic but not pulsed intracavity waveform. The left inset shows the optical spectrum resulting from cascaded FWM and illustrates how the superposition of comb frequencies (blue waves) with arbitrary phase (black arrows) results in a periodic intracavity power (red). The presence of a soliton implies synchronized phases and a pulsed intracavity power (right inset). a.u., arbitrary units.

pulses form spontaneously without the need for external stimulation. The number of solitons that circulate in the microresonator depends on the pump-laser detuning. The generated solitons remain stable until the pump laser is switched off without the need for active feedback on either the resonator or the pump laser. This remarkable stability in the presence of solitons is discussed below. Our discovery enables a c.w. laser beam to be converted into a train of femtosecond pulses, which corresponds to a low-noise smooth spectral envelope frequency comb in the time domain.

**$\text{MgF}_2$  microresonator.** In the present work, the  $\text{MgF}_2$  microresonator<sup>30–33</sup> used meets the basic requirements for temporal dissipative soliton formation, that is Kerr nonlinearity (also responsible for the parametric gain) and anomalous dispersion. The microresonator (Fig. 1a) was characterized by a FSR of 35.2 GHz and a coupled resonance width of  $\kappa/2\pi \approx 450$  kHz (see Methods). The measured (see Fig. 1b)<sup>34</sup> anomalous group-velocity dispersion (GVD) of the optical mode family used was  $\beta_2 \approx -9.39$  ps<sup>2</sup> km<sup>-1</sup>, which, in the context of microresonators, can be expressed conveniently in terms of the parameter<sup>22,35</sup>  $D_2 = -c/n_0 D_1^2 \beta_2 \approx 2\pi 16$  kHz that approximately describes the deviation of the resonance frequencies  $\omega_\mu = \omega_0 + D_1\mu + \frac{1}{2}D_2\mu^2 + \frac{1}{6}D_3\mu^3 + \dots$  from an equidistant frequency grid defined by  $\omega_0 + \mu D_1$ , where  $c$  is the speed of light,  $n_0$  the refractive index of  $\text{MgF}_2$  and  $\mu$  the relative mode number

with respect to the pumped mode  $\omega_0$  ( $\mu = 0$ ).  $D_1/2\pi$  is the FSR of the resonator at the frequency  $\omega_0$ . The frequency deviation increased quadratically with increasing relative mode number  $\mu$ , as evidenced in Fig. 1b;  $D_3$  and higher-order terms can be neglected in the present case.

**Search for solitons in a microresonator.** To search for soliton states in the microresonator, a pump laser (fibre laser, wavelength 1,553 nm; short-term linewidth 10 kHz) was scanned with decreasing optical frequency  $\omega_p$  over a high- $Q$  resonance of the crystalline  $\text{MgF}_2$  resonator. This approach was motivated because the pump-laser detuning is a critical parameter for the existence of cavity solitons<sup>34,36</sup>. Figure 2b shows the evolution of the optical spectrum during the laser scan. Reducing the laser-cavity detuning led to a build-up of intracavity power and, once a critical power threshold<sup>37,38</sup> was reached, widely spaced primary sidebands were generated by FWM, followed by secondary lines that filled in the spectral gaps, as frequently observed in FWM-based microresonator combs<sup>22,23,32</sup>. As the scan was performed, the radiofrequency (RF) signal (electronically down-mixed to 20 MHz) that resulted from the beating between neighbouring comb lines was sampled and Fourier transformed (Fig. 2c). A necessary signature of stable soliton formation is a low-noise narrow RF signal that results from the repetitive output-coupling of a soliton pulse. Indeed, we observed a transition from a broad, noisy RF signal to a single, low-noise RF beatnote for a particular laser detuning. This transition coincided with the beginning of a series of discrete steps in the transmission, which deviated markedly from the expected triangular resonance shape (the RF beatnote remained narrow throughout all the steps). Observations similar to the discrete transmission steps have been made in a  $\chi^{(2)}$  nonlinear microwave resonator, and were related to soliton formation<sup>39</sup>. To determine the effective pump-laser detuning, a Pound–Drever–Hall (PDH) signal was recorded as we scanned over the resonance. Strikingly, the first step, that is the transition to low noise, coincided with the zero crossing of the PDH signal, which marks the effective zero detuning frequency. This observation implies that the occurrence of the steps coincided with the transition from the effectively blue-detuned regime of microresonator-based FWM combs to the so far unexplored effectively red-detuned regime.

**Numerical simulation and analytical description of solitons in a microresonator.** To understand the intriguing observations of discrete steps in the transmission and the possible connection to soliton formation we carried out numerical simulations of a microresonator system with parameters similar to the experimental  $\text{MgF}_2$  resonator. The simulations were based on the coupled mode equations approach (see Methods)<sup>40</sup>. The coupled mode equations are equivalent to the Lugiato–Lefever equation when  $D_3$  and higher-order dispersions can be neglected<sup>10</sup>, which was the case in our microresonator (see Fig. 1b). The remaining resonator parameters were refractive and nonlinear indices, as well as the effective mode volume. We neglected effects of non-unity mode overlap, interactions with other mode families and any particularities of the resonator geometry and thermal effects. The resulting set of coupled mode equations was numerically propagated in time (see Methods and Supplementary Information Section I). Results of a numerical simulation, including 101 comb modes, are shown in Fig. 3. The blue curve in Fig. 3a shows the simulated average intracavity power as a function of the normalized detuning,  $\zeta_o = 2(\omega_0 - \omega_p)/\kappa$ , of the pump laser  $\omega_p$  from the cold resonance frequency  $\omega_0$ . The average intracavity power (the blue curve in Fig. 3a) is equivalent to the experimental transmission trace in Fig. 2a (an increased transmission corresponds to a decrease in intracavity power). Owing to the

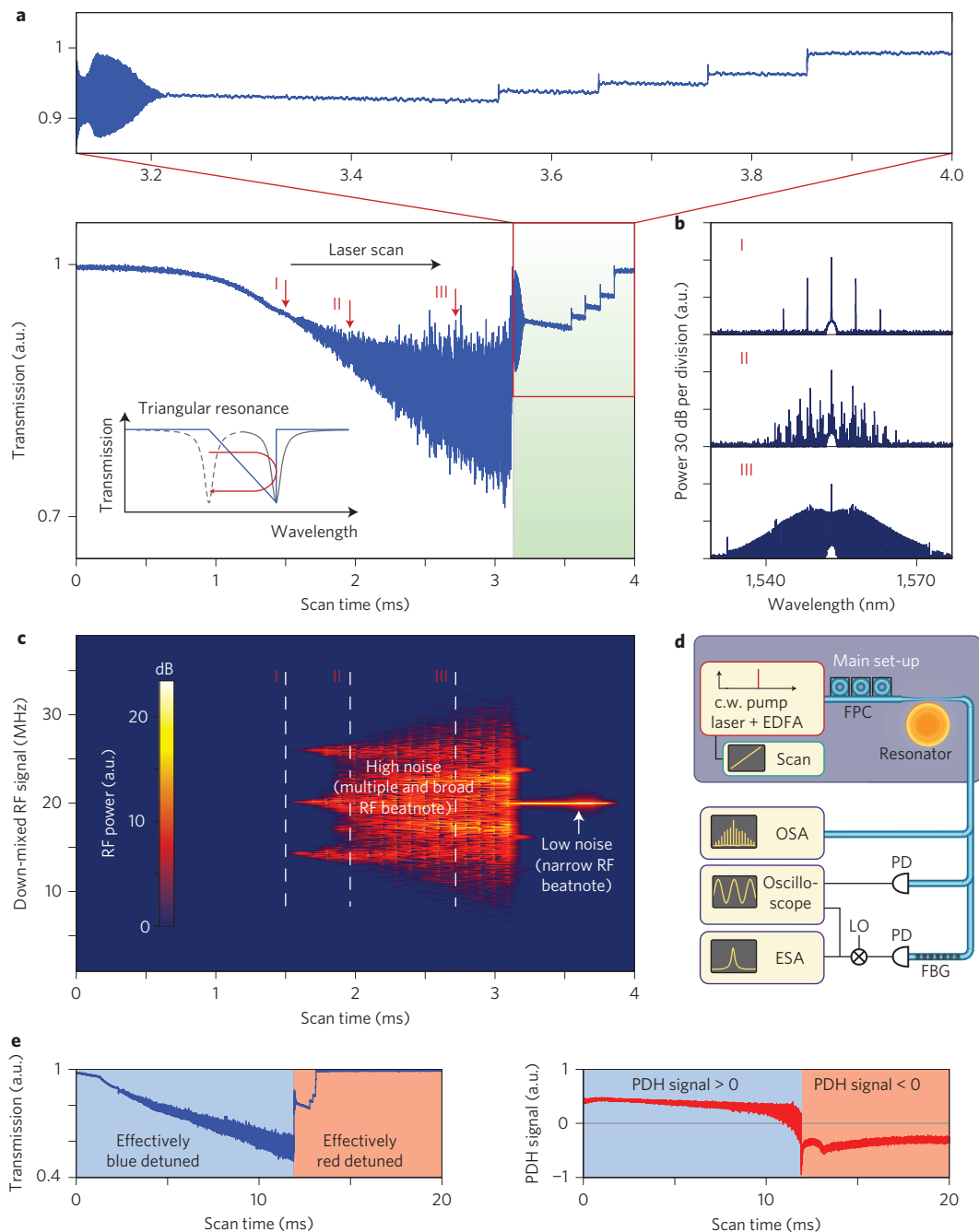


**Figure 2 | Transmission and beatnote.** **a**, Transmission observed when scanning a laser over a resonance of a high-Q Kerr-nonlinear  $\text{MgF}_2$  microresonator (coupled pump power 5 mW). The transmission signal follows the expected triangular resonance shape (see inset) with deviations in the form of discrete steps (green shading). **b**, Evolution of the optical power spectrum for three different positions in the scan; spectrum II and, in particular, the mesa-shaped spectrum III exhibit a high-noise RF beat signal. **c**, Down-mixed RF beat signal. **d**, Main experimental set-up composed of pump laser and resonator followed by an optical spectrum analyser (OSA), an oscilloscope to record the transmission and to sample the down-mixed beatnote (via the third harmonic of a local oscillator (LO) at 11.7 GHz), and an electrical spectrum analyser (ESA) to monitor the beatnote. Before beatnote detection the pump was filtered out by a narrow FBG in transmission (circulator and reflected beam dump not shown). FPC, fibre polarization controller; PD, photodetector; EDFA, erbium-doped fibre amplifier. **e**, Transmission and PDH error signal. Effective blue and red detunings are shaded blue and red, respectively.

Kerr-nonlinear shift of the resonance frequency, the effective detuning between the pump laser and resonance is smaller than  $\zeta_0$ . The step features are very well reproduced, which implies that the simulation includes all the relevant physical mechanisms. In agreement with the experiment (see Supplementary Information Section VIII) the number and height of steps fluctuated in repeated numerical scans. Numerically tracing out all possible comb evolutions yielded the orange curves in Fig. 3a, which

shows the multistability of the system (that is, many possible stable states for a given laser detuning). The first part of the evolution of the optical spectrum, shown in Fig. 3b, follows the known pathway for FWM-based comb formation<sup>22</sup>. Later on, with each step in the transmission the optical spectrum becomes less modulated until it eventually reaches a perfectly smooth envelope state (Fig. 3b, XI). An animation of the simulation is given in the Supplementary Information.

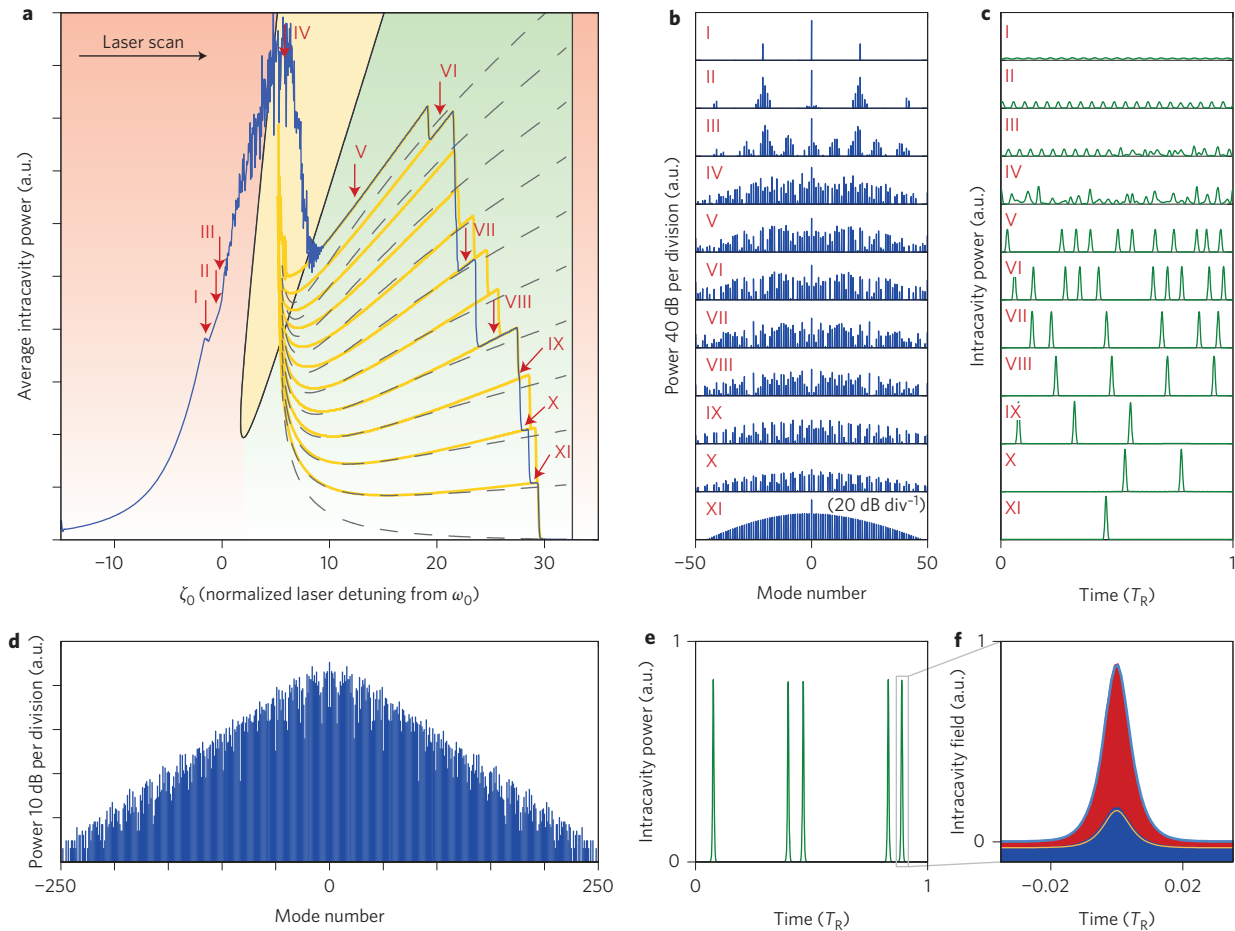


**Figure 3 | Numerical simulations of soliton formation in a microresonator.** **a**, Average intracavity power (blue, corresponding to the transmission signal in Fig. 2a when mirrored horizontally) during a simulated laser scan (101 simulated modes) over a resonance in a  $\text{MgF}_2$  resonator. The step features are well reproduced. The orange lines trace out all possible evolutions of the system during the scan. The dashed lines show an analytical description of the steps. The green area corresponds to the area in which solitons can exist, the yellow area allows for breather solitons with a time-variable envelope; solitons cannot exist in the red area. **b,c**, Optical spectra and intracavity powers for the different positions I–XI in the laser scan. **d**, Optical spectrum obtained when simulating 501 modes and stopping the simulated laser scan in the soliton regime. **e**, Intracavity power for the state in **d** with five solitons ( $T_R$  round-trip time). **f**, Enlargement of one of the solitons that shows the numerical results for the field real (red) and imaginary (dark blue) parts. The respective analytical soliton solutions are shown as light blue and orange lines.

To reveal the potential that underlies soliton formation we investigated the time-dependent intracavity power in Fig. 3c by phase coherently adding the individual simulated optical modes. Indeed, the first step (Fig. 3c, V) corresponds to a transition to a state in which multiple stable pulses propagate inside the cavity. Further steps can be associated with a switching behaviour where individual pulses are removed in a discrete manner. The separation between multiple pulses in the resonator is random. To confirm the soliton nature of these pulses we performed a simulation of 501 modes (Fig. 3d–f) and analysed a state of five pulses. We compared the numerical simulation with an approximate analytical solution of the Lugiato–Lefever equation<sup>5</sup>. For multiple solitons the analytical solution<sup>3</sup> has the form

$$\Psi(\phi) \approx C_1 + C_2 \sum_{j=1}^N \text{sech} \left( \sqrt{\frac{2(\omega_0 - \omega_p)}{D_2}} (\phi - \phi_j) \right) \quad (1)$$

where  $\Psi$  denotes the complex field amplitude,  $\phi$  the angular coordinate inside the resonator,  $\phi_j$  the angular coordinate of the  $j$ th soliton and  $N$  the number of solitons. The complex numbers  $C_1$  and  $C_2$  are determined fully by the resonator parameters and the pump conditions, and the ratio  $|C_2|^2/|C_1|^2$  of the soliton peak

power to the c.w. background can typically exceed several hundred (see Supplementary Information Section II for details). Indeed, the close-to-perfect match between the analytic solution and numerical results shows that the pulses forming in the microresonator were stable temporal dissipative cavity solitons. These solitons emerged from the modulated intracavity waveform, which may explain their spontaneous formation, in contrast to fibre cavities for which stimulating writing pulses are required<sup>4</sup>. From equation (1) it follows that the temporal width of the soliton decreases for increased normalized detuning  $\zeta_0$  and the estimated minimal temporal width (full-width at half-maximum (FWHM)) in a critically coupled resonator is

$$\Delta t_{\min}^{\text{FWHM}} \approx 2 \sqrt{\frac{-\beta_2}{\gamma \mathcal{F} P_{\text{in}}}} \quad (2)$$

where  $\mathcal{F}$  is the cavity's finesse,  $P_{\text{in}}$  the coupled pump power,  $\beta_2$  the GVD and  $\gamma = (\omega/c)(n_2/A_{\text{eff}})$  the effective nonlinearity with the nonlinear mode area  $A_{\text{eff}}$  and nonlinear refractive index  $n_2$  (see Supplementary Information Section V).

Having shown the soliton nature of the pulses in numerical simulation, we can interpret the blue curve in Fig. 3a based on



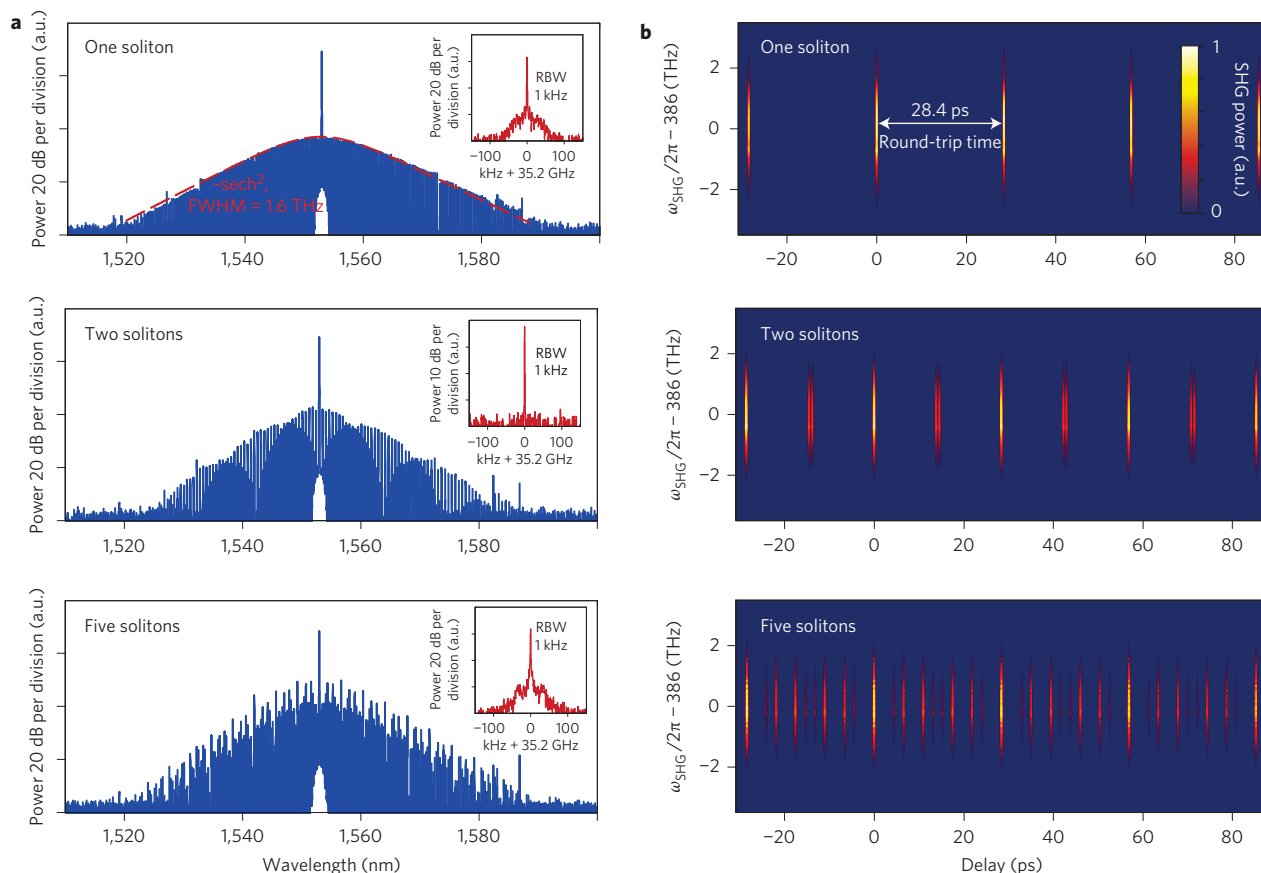


**Figure 4 | Experimental demonstration of stable temporal solitons in an optical microresonator. a**, Optical spectra of three selected states with one, two and five solitons, respectively. The insets show the RF beatnote, which is resolution-bandwidth limited to a 1 kHz width in all cases. The dashed red line in the optical spectrum of the one-pulse state shows the spectral  $\text{sech}^2$  envelope expected for solitons with a 3 dB bandwidth of 1.6 THz. **b**, FROG traces of the states in **a** that display the signal of the single and multiple pulses. (The FROG set-up is shown in Fig. 5b.)

general limits<sup>36</sup> that apply to solitons as solutions of the Lugiato–Lefever equation. Adopting these criteria for the present case we identify three main regions in Fig. 3a, coloured red, yellow and green (see Supplementary Information Section III). Solitons with a constant temporal envelope can only exist in the green area. The yellow area still allows for solitons with a time-varying envelope ('breather solitons'<sup>41</sup>), but solitons cannot exist in the red areas. In the red area on the left of Fig. 3a, the system may undergo chaotic Hopf bifurcations<sup>36</sup>. The correspondence of these analytical limits with the numerical results is remarkable.

For different numbers of solitons we can derive the average power inside the resonator by averaging the respective analytic soliton solution (equation (1)) over one cavity round-trip time. This analytical result is shown as dark-grey dashed lines in Fig. 3a, and is in excellent agreement with the numerically observed steps (to account for the limitation caused by the low mode number in the simulation an additional correction factor of order unity was applied). The intracavity power changed discontinuously with the number of solitons present in the cavity (see Supplementary Information Section IV).

**Experimental demonstration of stable solitons in a microresonator.** The challenge in experimentally generating soliton states is the thermally induced resonance shift that acts in addition to the Kerr-nonlinear resonance shift, but on a much slower timescale (thermal relaxation time). If the soliton state is reached but the resonator is not in thermal equilibrium (which depends on the average intracavity power), then the temperature of the resonator will change, which will affect the effective

detuning and destabilize the system. It is thus important that the soliton state is reached with the resonator being close to its equilibrium temperature. As we detail in the Supplementary Information (Section VI) this is possible if the laser is tuned into the soliton state with an appropriately chosen tuning speed. In this way, once generated, the solitons remain stable until the pump laser is switched off and no active feedback on either the resonator or the pump laser is required.

Regardless of reaching the soliton state in thermal equilibrium, it is remarkable that the system remains self-stable as usually the resonator cannot be operated effectively red detuned with a significant intracavity power<sup>29</sup>. In the following, we explain qualitatively that the self-stability of the system can be attributed to the presence of solitons. In the case of a pulsed intracavity waveform, different fractions of the pump light experience different Kerr-nonlinear phase shifts during one round trip. The small spatial fraction of the pump light that propagates overlapping with the high-intensity soliton inside the resonator experiences a much larger nonlinear phase shift compared to the light propagating with the weak c.w. background field. Although the main fraction of the pump light is effectively far-red detuned (and dominates the PDH signal, Fig. 2e), the small fraction that overlaps with the soliton inside the resonator is effectively blue detuned, which permits a high soliton power. The blue-detuned soliton component is evidenced by the series of steps that correspond to a set of small triangular resonances, which are characteristic of blue detuning (one triangle per realized soliton state, as shown in Figs 2a and 3a). Thus, considering the Kerr-nonlinear resonance shift, a soliton state can be interpreted as a superposition of two stable solutions<sup>29</sup>, effectively blue detuned

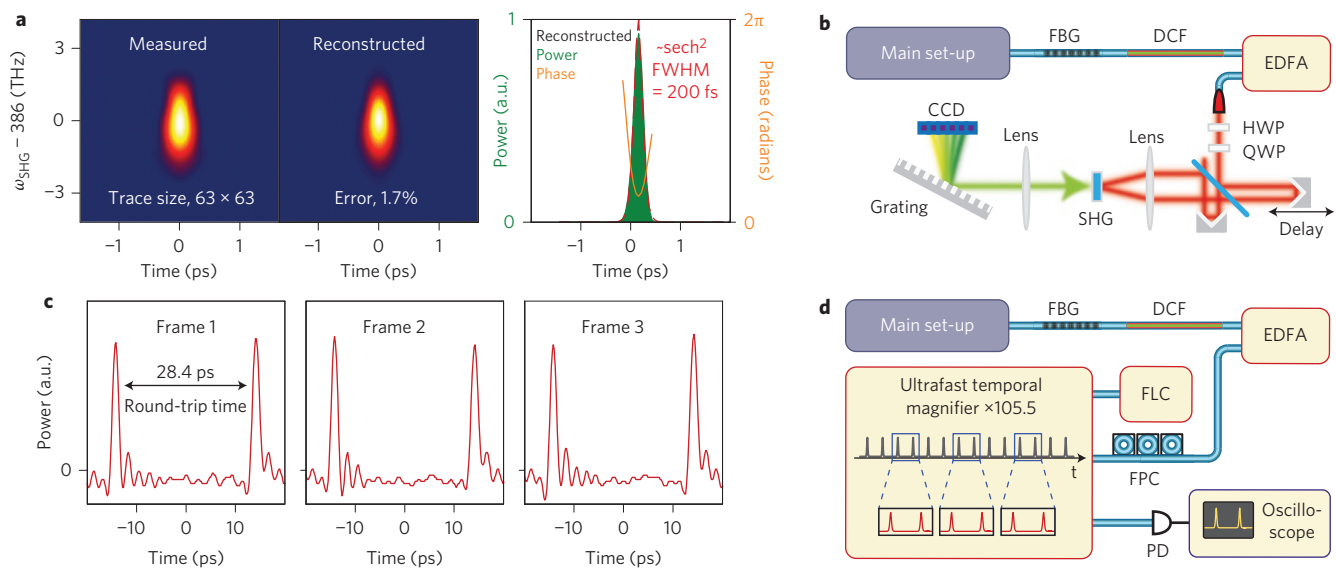


**Figure 5 | Temporal characterization of ultrashort pulses.** **a**, Higher-resolution experimental FROG trace of a one-soliton pulse (left, colour scale same as in Fig. 4b). The reconstruction (middle) converges to a FROG error of  $\varepsilon \approx 1.7\%$ , in good agreement with the experimental trace. The reconstruction (right) of power and phase yields an estimated pulse duration of 200 fs (FWHM). **b**, Set-up of the FROG experiment. **c**, Sampled optical power of the microresonator output over a duration of 40 ps. The three measurements (frames 1, 2 and 3) are separated from one another by a duration of 4 ns, which corresponds to  $\sim 140$  round-trip times of 28.4 ps. The smaller trailing peaks can be attributed to ringing in the photodetection circuit. **d**, Set-up of the power sampling experiment, including the PicoLuz LLC temporal magnifier and a 4 GHz sampling oscilloscope. FBG is in transmission (circulator and reflected beam dump not shown). FLC, fibre laser comb (250 MHz repetition rate); HWP, half-wave plate; QWP, quarter-wave plate; DCF, dispersion-compensating fibre.

(high-power solitons) and red detuned (low-power c.w. background), realized at the same time. In contrast to the fast Kerr effect, the thermal resonance shift is slow compared to the cavity round-trip time and only depends on the averaged intracavity power. In the microresonator the detuning-dependent change of the averaged intracavity power is dominated by the effectively blue-detuned soliton component, as opposed to the effectively red-detuned c.w. component (see Figs 2a and 3a). This implies that, with respect to the slow thermal effect, the resonator behaves as being effectively blue detuned and thus self-stable<sup>29</sup>. A more detailed discussion is given in Supplementary Information Section VII.

Having access to the stable operation of these soliton states, we investigated experimentally (in addition to their RF beatnote and optical spectrum (Fig. 4a)) their temporal characteristics by performing a frequency-resolved optical gating (FROG) experiment (Fig. 4b). This corresponds to a second-harmonic generation (SHG) autocorrelation experiment in which the frequency-doubled light is resolved spectrally (Fig. 5b and Methods). In contrast to autocorrelation, the FROG method (when combined with measurements of the RF beatnote) allows a reliable identification of ultrashort pulses via the associated minimal bandwidth of the SHG spectrum given by the time–bandwidth product (TBP). A comparison of autocorrelation and the FROG method is provided in Supplementary Information Section IX.

In full consistency with the numerical simulations, single and multiple soliton states were observed. The single soliton state was characterized by a smooth spectral envelope, without spectral gaps. The power spectral envelope exhibited a  $\text{sech}^2$  shape (3 dB bandwidth, 1.6 THz corresponding to more than 45 modes) as expected from the Fourier transform of the temporal field envelope. Based on the TBP for solitons of 0.315 (see Supplementary Information Section V), the expected pulse duration is 197 fs. The observed RF beatnote with low phase noise was resolution-bandwidth limited to 1 kHz and its signal-to-noise ratio exceeded 60 dB. The FROG trace shows a train of pulses well separated by the cavity round-trip time of 28.4 ps, which corresponds to the FSR of 35.2 GHz. The multisoliton states (here shown for the case

of two and five solitons) show a more structured optical spectrum. This structure reflects the number and distribution of solitons in the cavity (see Supplementary Information Section V). The RF beatnote generated in the multisoliton states is of similar quality to that in the single-soliton state. Importantly, the FROG measurement allows for a full reconstruction (neglecting a time-direction ambiguity) of power and phase of the pulses (see Fig. 5a). The reconstructed  $\text{sech}^2$  shaped power profile is consistent with the expectation for solitons and the reconstructed temporal width of 200 fs (FWHM) is in agreement with the bandwidth of the optical spectrum and the expectation based on equation (2).

To further corroborate the presented results, an independent power sampling method was applied to a single-soliton state. The high repetition rate prohibits direct sampling, which would require a bandwidth of hundreds of gigahertz for detection and recording. This limitation can be overcome by stretching the optical waveform in time using the time lens effect<sup>42</sup> (Fig. 5d; ultrafast temporal magnifier, PicoLuz LLC). Although the time resolution of about 2.5 ps does not allow the duration of the pulse to be determined, this single-shot method, unlike autocorrelation-type experiments, does not rely on averaging. The results in Fig. 5c clearly show optical pulses, separated by the cavity round-trip time with constant pulse amplitudes, as expected for temporal dissipative solitons. We emphasize that in all the temporal characterization experiments neither phase and amplitude adjustment nor spectral filtering was applied (except for pump suppression). The latter proves that the full spectrum contributes to the pulse in contrast to only a spectrally limited contribution of a sub-comb<sup>22</sup>. The gain window ( $\geq 4$  THz) of the optical amplifier used before temporal characterization supports more than 100 comb modes.

## Discussion

Combining experimental, numerical and analytical results, we have demonstrated the spontaneous formation of temporal dissipative solitons in a  $\text{MgF}_2$  microresonator. The temporal width of the soliton depends on the pump power and the dispersion of the resonator (see equation (2)). In the present case the optical pulses were

in the range 100–200 fs (see Supplementary Information Section XI). Given the possibility of dispersion engineering<sup>32,43</sup> in microresonators and the broadband<sup>25,44</sup> nature of the parametric gain, significantly shorter pulses are conceivable. As our results depend only on the generic properties of Kerr-nonlinear microresonators with anomalous dispersion, they apply equally to other microresonator comb platforms. Soliton formation may also explain the generation of femtosecond pulses in Si<sub>3</sub>N<sub>4</sub> resonators<sup>26</sup> reported recently. Moreover, our results are in agreement with very recent numerical work on soliton formation in microresonators<sup>45–47</sup>. Temporal dissipative solitons in microresonators, in combination with chip-scale<sup>15,16</sup> integration, open the route towards compact, stable and low-cost ultrashort pulse sources<sup>2</sup>, which can also operate in wavelength regimes (such as the mid-infrared<sup>33</sup>) where broadband laser-gain media or saturable absorbers do not exist. In contrast to mode-locked lasers, which rely on a different gain mechanism, no additional element, such as a saturable absorber, is required for stable operation in the microresonator case (see Supplementary Information Section X). Moreover, femtosecond pulses in conjunction with external broadening (see Supplementary Information Section XI for a first demonstration) provide a viable route to a microresonator RF-to-optical link<sup>48</sup>. In the frequency domain, solitons enable microresonator-based combs with low noise and smooth spectral envelopes. These low-noise spectra with unprecedentedly small line-to-line power variations are essential to frequency-domain application in telecommunications, broadband spectroscopy and astronomy<sup>17</sup>. The stability of dissipative solitons<sup>2</sup> is also of interest to low phase-noise microwave generation<sup>14</sup>. Besides practical applications, solitons in microresonators are novel platforms for studying soliton physics, such as the interaction between solitons<sup>49</sup> or soliton crystals<sup>1,2</sup>.

## Methods

**Experimental set-up and parameters.** The pump laser (fibre laser, 1,553 nm wavelength, short-term linewidth <10 kHz) was amplified by an erbium-doped fibre amplifier (EDFA) and evanescently coupled to the MgF<sub>2</sub> resonator (FSR 35.2 GHz, refractive index  $n_0 \approx 1.37$ ) via a tapered optical fibre. The coupled resonance width of  $\kappa/2\pi \approx 450$  kHz (quality factor  $Q \approx 4 \times 10^8$ , finesse  $\mathcal{F} \approx 78 \times 10^4$ ) was measured using modulation sidebands of a scanning laser. The dispersion of the resonator was found, following the method of Del'Haye *et al.*<sup>34</sup>, to be  $D_2/2\pi \approx 16$  kHz, that is  $\beta_2 \approx -9.39$  ps<sup>2</sup> km<sup>-1</sup>. A typical coupled pump power of  $P_{\text{in}} \approx 5$ –30 mW led to circulating powers of several hundreds of watts. The estimated effective mode area,  $A_{\text{eff}} \approx 90 \times 10^{-12}$  m<sup>2</sup> (effective mode volume  $V_{\text{eff}} \approx 5.6 \times 10^{-13}$  m<sup>3</sup>), and the nonlinear refractive index,  $n_2 \approx 0.9 \times 10^{-20}$  m<sup>2</sup> W<sup>-1</sup>, yielded an estimated nonlinear parameter of

$$\gamma = \frac{\omega_p n_2}{c A_{\text{eff}}} \approx 4.1 \times 10^{-4} \text{ m}^{-1} \text{ W}^{-1}$$

**Numerical simulation.** The simulations are based on the coupled mode equations (see Supplementary Information Section I), which are numerically propagated in time using an adaptive step-size Runge–Kutta integrator. The initial FWM processes were seeded by simulated zero point fluctuations in the mode amplitudes. The simulated resonator was defined similarly to the experimental resonator by its resonance frequencies  $\omega_\mu$  given by  $D_1/2\pi = 35.2$  GHz,  $D_2/2\pi = 10$  kHz,  $D_3/2\pi = -130$  Hz (these values were measured for a resonator similar to the one used here) and a quality factor of  $Q = 2 \times 10^8$  for critical coupling. All other parameters were equal to the values listed for the experimental resonator. The coupled pump power was set to  $P_{\text{in}} = 100$  mW at a pump frequency of  $\omega_p/2\pi = 193$  THz. Short, simulated pump-power drops (duration  $2\pi/\kappa$ ; relative amplitude 50–100%) can be used to induce transitions between different soliton states and the scan direction can be reversed at any time with a precise knowledge of laser detuning. Induced state transitions and reversed tuning directions were used to trace out the orange curves in Fig. 3a.

**FROG experiment.** Prior to the FROG experiment, the optical spectra were sent through a fibre Bragg grating (FBG) for pump suppression (–30 dB) and subsequently amplified to 50 mW. Dispersion-compensating fibre (Thorlabs DCF3, DCF38) was used to approximately compensate the dispersion. In the FROG set-up (see Fig. 5b) the generated optical pulses were split interferometrically and recombined with a variable delay in a nonlinear barium borate (BBO) crystal. This resulted in SHG whenever the optical pulses in the two arms of the interferometer overlapped temporally in the BBO crystal. The generated SHG light was resolved

spectrally and recorded as a function of delay by a CCD (charge-coupled device) spectrometer to yield a FROG trace. Each FROG trace consisted of nearly 1,000 spectra with individual exposure times of 800 ms. The  $N \times N$  ( $N = 63$ ) FROG trace of the single pulse state in Fig. 5a was analysed using a principal component generalized projection algorithm<sup>50</sup>, after noise removal via Fourier filtering. The FROG reconstruction error is defined as

$$\varepsilon = \frac{1}{N} \sqrt{\sum_{i,j}^N (M_{ij}^{\text{meas}} - M_{ij}^{\text{reco}})^2}$$

where  $M_{ij}^{\text{meas}}$  and  $M_{ij}^{\text{reco}}$  denote the elements of the  $N \times N$  matrices that represent the measured and reconstructed FROG traces. With regard to the interpretation of the FROG traces, a number of  $n$  pulses create  $(2n - 1)$  peaks (as a function of delay) in the FROG trace. The separation of the pulses can be reconstructed by a deconvolution, the major peak results from the fact that all pulses overlap (when the delay is an integer multiple of the round-trip time) and the minor peaks result from overlap between a reduced number of pulses.

Received 10 July 2013; accepted 16 November 2013;  
published online 22 December 2013

## References

- Akhmediev, N. & Ankiewicz, A. *Dissipative Solitons: From Optics to Biology and Medicine* (Springer, 2008).
- Grelu, P. & Akhmediev, N. Dissipative solitons for mode-locked lasers. *Nature Photon.* **6**, 84–92 (2012).
- Wabnitz, S. Suppression of interactions in a phase-locked soliton optical memory. *Opt. Lett.* **18**, 601–603 (1993).
- Leo, F. *et al.* Temporal cavity solitons in one-dimensional Kerr media as bits in an all-optical buffer. *Nature Photon.* **4**, 471–476 (2010).
- Lugiato, L. A. & Lefever, R. Spatial dissipative structures in passive optical systems. *Phys. Rev. Lett.* **21**, 2209–2211 (1987).
- Nozaki, K. & Bekki, N. Low-dimensional chaos in a driven damped nonlinear Schrödinger equation. *Physica D* **21**, 381–393 (1986).
- Segev, M. & Stegeman, G. Self-trapping of optical beams: spatial solitons. *Phys. Today* **51**, August, 42–48 (1998).
- Barland, S., Tredicce, J. R. & Brambilla, M. Cavity solitons as pixels in semiconductor microcavities. *Nature* **419**, 699–702 (2002).
- Firth, W. J. & Weiss, C. O. Cavity and feedback solitons. *Opt. Photon. News* **13**, 54–58 (2002).
- Matsko, A. B. *et al.* Mode-locked Kerr frequency combs. *Opt. Lett.* **36**, 2845–2847 (2011).
- Vahala, K. J. Optical microcavities. *Nature* **424**, 839–846 (2003).
- Braginsky, V. B., Gorodetsky, M. L. & Ilchenko, V. S. Quality-factor and nonlinear properties of optical whispering-gallery modes. *Phys. Lett. A* **137**, 393–397 (1989).
- Del'Haye, P. *et al.* Optical frequency comb generation from a monolithic microresonator. *Nature* **450**, 1214–1217 (2007).
- Savchenkov, A. A. *et al.* Tunable optical frequency comb with a crystalline whispering gallery mode resonator. *Phys. Rev. Lett.* **101**, 93902 (2008).
- Levy, J. S. *et al.* CMOS-compatible multiple-wavelength oscillator for on-chip optical interconnects. *Nature Photon.* **4**, 37–40 (2010).
- Razzari, L. *et al.* CMOS-compatible integrated optical hyper-parametric oscillator. *Nature Photon.* **4**, 41–45 (2010).
- Kippenberg, T. J., Holzwarth, R. & Diddams, S. A. Microresonator-based optical frequency combs. *Science* **332**, 555 (2011).
- Papp, S., Del'Haye, P. & Diddams, S. Mechanical control of a microrod-resonator optical frequency comb. *Phys. Rev. X* **3**, 031003 (2013).
- Li, J., Lee, H., Chen, T. & Vahala, K. J. Low-pump-power, low-phase-noise, and microwave to millimeter-wave repetition rate operation in microcombs. *Phys. Rev. Lett.* **109**, 233901 (2012).
- Del'Haye, P., Arcizet, O., Schliesser, A., Holzwarth, R. & Kippenberg, T. J. Full stabilization of a microresonator-based optical frequency comb. *Phys. Rev. Lett.* **101**, 53903 (2008).
- Del'Haye, P., Papp, S. B. & Diddams, S. A. Hybrid electro-optically modulated microcombs. *Phys. Rev. Lett.* **109**, 263901 (2012).
- Herr, T. *et al.* Universal formation dynamics and noise of Kerr-frequency combs in microresonators. *Nature Photon.* **6**, 480–487 (2012).
- Ferdous, F. *et al.* Spectral line-by-line pulse shaping of on-chip microresonator frequency combs. *Nature Photon.* **5**, 770–776 (2011).
- Papp, S. B. & Diddams, S. A. Spectral and temporal characterization of a fused-quartz-microresonator optical frequency comb. *Phys. Rev. A* **84**, 53833 (2011).
- Del'Haye, P. *et al.* Octave spanning tunable frequency comb from a microresonator. *Phys. Rev. Lett.* **107**, 063901 (2011).
- Saha, K. *et al.* Modelocking and femtosecond pulse generation in chip-based frequency combs. *Opt. Express* **21**, 1335–1343 (2013).

27. Peccianti, M. *et al.* Demonstration of a stable ultrafast laser based on a nonlinear microcavity. *Nature Commun.* **3**, 765 (2012).
28. Ilchenko, V. S. & Gorodetsky, M. L. Thermal nonlinear effects in optical whispering gallery microresonators. *Laser Phys.* **2**, 1004–1009 (1992).
29. Carmon, T., Yang, L. & Vahala, K. J. Dynamical thermal behavior and thermal selfstability of microcavities. *Opt. Express* **12**, 4742–4750 (2004).
30. Grudin, I. *et al.* Ultra high Q crystalline microcavities. *Opt. Commun.* **265**, 33–38 (2006).
31. Liang, W. *et al.* Generation of near-infrared frequency combs from a MgF<sub>2</sub> whispering gallery mode resonator. *Opt. Lett.* **36**, 2290–2292 (2011).
32. Grudin, I. S., Baumgartel, L. & Yu, N. Frequency comb from a microresonator with engineered spectrum. *Opt. Express* **20**, 6604–6609 (2012).
33. Wang, C. *et al.* Mid-infrared optical frequency combs at 2.5  $\mu\text{m}$  based on crystalline microresonators. *Nature Commun.* **4**, 1345 (2013).
34. Del'Haye, P., Arcizet, O., Gorodetsky, M. L., Holzwarth, R. & Kippenberg, T. J. Frequency comb assisted diode laser spectroscopy for measurement of microcavity dispersion. *Nature Photon.* **3**, 529–533 (2009).
35. Savchenkov, A. A. *et al.* Kerr combs with selectable central frequency. *Nature Photon.* **5**, 293–296 (2011).
36. Barashenkov, I. V. & Smirnov, Y. S. Existence and stability chart for the ac-driven, damped nonlinear Schrödinger solitons. *Phys. Rev. E* **54**, 5707–5725 (1996).
37. Kippenberg, T. J., Spillane, S. M. & Vahala, K. J. Kerr-nonlinearity optical parametric oscillation in an ultrahigh-Q toroid microcavity. *Phys. Rev. Lett.* **93**, 83904 (2004).
38. Matsko, A. B., Savchenkov, A. A., Strekalov, D., Ilchenko, V. S. & Maleki, L. Optical hyperparametric oscillations in a whispering-gallery-mode resonator: threshold and phase diffusion. *Phys. Rev. A* **71**, 33804 (2005).
39. Gasch, A., Wedding, B. & Jäger, D. Multistability and soliton modes in nonlinear microwave resonators. *Appl. Phys. Lett.* **44**, 1105–1107 (1984).
40. Chembo, Y. K. K. & Yu, N. Modal expansion approach to optical-frequency-comb generation with monolithic whispering-gallery-mode resonators. *Phys. Rev. A* **82**, 33801 (2010).
41. Matsko, A., Savchenko, A. & Maleki, L. On excitation of breather solitons in an optical microresonator. *Opt. Lett.* **37**, 4856–4858 (2012).
42. Salem, R. *et al.* High-speed optical sampling using a silicon-chip temporal magnifier. *Opt. Express* **17**, 4324–4329 (2009).
43. Riemensberger, J. *et al.* Dispersion engineering of thick high-Q silicon nitride ring-resonators via atomic layer deposition. *Opt. Express* **20**, 770–776 (2012).
44. Okawachi, Y. *et al.* Octave-spanning frequency comb generation in a silicon nitride chip. *Opt. Lett.* **36**, 3398–3400 (2011).
45. Coen, S., Randle, H. G., Sylvestre, T. & Erkintalo, M. Modeling of octave-spanning Kerr frequency combs using a generalized mean-field Lugiato–Lefever model. *Opt. Lett.* **38**, 37–39 (2013).
46. Coen, S. & Erkintalo, M. Universal scaling laws of Kerr frequency combs. *Opt. Lett.* **38**, 1790–1792 (2013).
47. Chembo, Y. K. & Menyuk, C. R. Spatiotemporal Lugiato–Lefever formalism for Kerr-comb generation in whispering-gallery-mode resonators. *Phys. Rev. A* **87**, 053852 (2013).
48. Cundiff, S. T. & Ye, J. Colloquium: femtosecond optical frequency combs. *Rev. Modern Phys.* **75**, 325–342 (2003).
49. Jang, J. K., Erkintalo, M., Murdoch, S. G. & Coen, S. Ultraweak long-range interactions of solitons observed over astronomical distances. *Nature Photon.* **7**, 657–663 (2013).
50. Kane, D. J. Principal components generalized projections: a review. *J. Optic. Soc. Am. B* **25**, A120–A132 (2008).

## Acknowledgements

The authors thank R. Salem and A. Gaeta for providing the PicoLuz LLC ultrafast temporal magnifier and advice when evaluating the data. The authors acknowledge valuable advice by K. Hartinger on dispersion compensation as well as helpful discussion with S. Coen and M. Erkintalo. This work was supported by the DARPA program QuASAR, the Swiss National Science Foundation. V.B. acknowledges support by an ESA PhD fellowship. J.D.J. acknowledges support by Marie Curie IIF. M.L.G. acknowledges support from RFBR grant 13-02-00271 and partial support by State Contract 07.514.12.4032. The research that led to these results received funding from the European Union Seventh Framework Programme (FP7/2007–2013) under grant agreement No. 263500.

## Author contributions

T.H. designed and performed the experiments and analysed the data. M.L.G. and T.H. performed the numerical simulations, M.L.G. developed the analytic description, V.B. assisted in the experiments, J.D.J. assisted in the temporal magnifier experiment, T.H. and M.L.G. fabricated the sample, C.Y.W. assisted in sample fabrication and N.M.K. assisted in developing the analytic description. T.H., M.L.G. and T.J.K. wrote the manuscript. T.J.K. supervised the project.

## Additional information

Supplementary information is available in the online version of the paper. Reprints and permissions information is available online at [www.nature.com/reprints](http://www.nature.com/reprints). Correspondence and requests for materials should be addressed to M.L.G. and T.J.K.

## Competing financial interests

The authors declare no competing financial interests.